# Observation of topological $\mathbb{Z}_2$ vortex fluctuations in the frustrated Heisenberg magnet $NaCrO_2$

K. Tomiyasu,[1,2,*] Y. P. Mizuta,[3] M. Matsuura,[4] K. Aoyama,[5] and H. Kawamura[6,†]

[1]*Department of Physics, Tohoku University, Aoba, Sendai 980-8578, Japan*
[2]*Nissan ARC Ltd., Natsushima-cho 1, Yokosuka 237-0061, Japan*
[3]*Graduate School of Engineering Science, Osaka University, Toyonaka, Osaka 560-8531, Japan*
[4]*CROSS Neutron Science and Technology Center, IQBRC Building, Tokai, Ibaraki 319-1106, Japan*
[5]*Department of Earth and Space Science, Graduate School of Science, Osaka University, Osaka 560-0043, Japan*
[6]*Molecular Photoscience Research Center, Kobe University, Kobe 657-8501, Japan*

(Received 29 October 2021; accepted 6 July 2022; published 2 August 2022)

Spin fluctuations in the triangular-lattice Heisenberg antiferromagnet $NaCrO_2$ are investigated by means of quasielastic neutron scattering with high energy resolution and a wide energy band. Two components with the following features are captured separately. They are pronounced at intermediate temperatures of 20–50 K. One, with quite an extended lifetime corresponding to $\sim 0.001 E_{ex}$ ($E_{ex}$ is the exchange energy), nearly disappears at low temperature (10 K), and the other, with an extended lifetime of $\sim 0.01 E_{ex}$, survives there, identified as the free $\mathbb{Z}_2$ vortex and $\mathbb{Z}_2$-vortex pair, respectively, in agreement with the $\mathbb{Z}_2$-vortex theory.

DOI: 10.1103/PhysRevB.106.054407

## I. INTRODUCTION

The magnetic vortex, a topologically stable nanoscale spin structure object in an easy-plane magnet, has attracted much attention from both fundamental and application perspectives. The standard vortex is characterized by the winding number $n = 0, \pm 1, \pm 2, \ldots$, the set corresponding to integers [$\mathbb{Z}$], where each $n$ forms a distinct topological sector [1]. Some time ago, Kawamura and Miyashita theoretically predicted that the frustrated *isotropic* Heisenberg magnets in two dimensions could possess a different type of vortex characterized by the paritylike two-valued topological number [$\mathbb{Z}_2$] corresponding only to its presence or absence, a $\mathbb{Z}_2$ vortex [2,3]. The noncollinear $SO(3) \equiv RP_3$ nature of the underlying spin correlation caused by frustration guarantees its topological stability via the relation $\Pi_1[SO(3)] = \mathbb{Z}_2$.

It was argued that the frustrated two-dimensional (2D) Heisenberg magnets exhibit a topological transition at a finite temperature $T = T_V$ driven by the binding and unbinding of the $\mathbb{Z}_2$ vortices [2–5]. In sharp contrast to the Kosterlitz-Thouless transition [1], the spin-correlation length remains finite even below $T_V$, and the low-$T$ state is a spin paramagnetic state with slow spin fluctuations characterized by the topologically broken ergodicity, dubbed a "spin-gel" state [3,4]. Interestingly, the finite spin-correlation length makes the $\mathbb{Z}_2$-vortex physics robust against weak perturbations like the weak three-dimensionality, the weak magnetic anisotropy, etc., which inevitably exist in real magnets. Further, a recent theory showed that a free $\mathbb{Z}_2$ vortex is capable of efficiently carrying spin density in connection with potential application of spintronics [6].

However, the experimental observation of a $\mathbb{Z}_2$ vortex has been quite difficult and, in fact, has remained elusive for years. In theory, the thermodynamic anomaly is extremely weak; for example, specific heat and magnetic susceptibility exhibit only a rounded nonsingular maximum slightly above $T_V$, whereas an essential singularity occurring at $T = T_V$ is probably too weak to experimentally detect [2–4]. Further, much experimental evidence, including specific heat [7,8], magnetic susceptibility [7–10], electron spin resonance (ESR) [11–15], nuclear magnetic resonance (NMR; nuclear quadrupole resonance) [8,16], muon spin resonance ($\mu$SR) [8,9,16–19], neutron scattering [7,10,20], and optical measurements [21], was accumulated for several materials but was entirely indirect in the sense of observing a free $\mathbb{Z}_2$ vortex separately from a $\mathbb{Z}_2$-vortex pair, which is the key ingredient to verify the $\mathbb{Z}_2$-vortex theory.

According to the theory, the $\mathbb{Z}_2$ vortices dynamically emerge, with binding and unbinding, in the intermediate temperature range around $T_V$ [2–5]. A free $\mathbb{Z}_2$ vortex is generated only above $T_V$ via the unbinding of the $\mathbb{Z}_2$-vortex pairs which exist both below and above $T_V$ and exhibits diffusive motion with a long lifetime. Note that the free $\mathbb{Z}_2$ vortex is a topologically protected object, so it can be annihilated only by a collision with other free $\mathbb{Z}_2$ vortices. Since there are few free $\mathbb{Z}_2$ vortices just above $T_V$, the free-vortex lifetime is expected to be quite long there, while well above $T_V$, where many free $\mathbb{Z}_2$ vortices are generated, the mutual collision between them occurs frequently and their lifetime is expected to become shorter. Since the $\mathbb{Z}_2$-vortex-pair unbinding process is expected to occur most frequently around the specific-heat-peak temperature $T_{Cp}$, $T_{Cp}$ might give a measure of the upper-bound temperature for the presence of the long-lived isolated free $\mathbb{Z}_2$ vortex. It was also simulated that a direct signature of a free $\mathbb{Z}_2$ vortex might be detectable as a quasielastic scattering in the energy spectrum at $T$'s between $T_V$ and $T_{Cp}$ [22].

*k.tomiyasu.sci@gmail.com
†h.kawamura.handai@gmail.com

 

Thus, in this study, we search for spin fluctuations in the intermediate temperature range by means of quasielastic neutron scattering (QENS), known as a powerful method to observe spin fluctuations. We then find in the intermediate temperature range of 20–50 K two QENS components with extended lifetimes: one with quite an extended lifetime corresponding to $\sim 0.001 E_{ex}$ ($E_{ex}$ is the exchange energy) which disappears at low temperatures ($\lesssim$10 K) and one with an extended lifetime of $\sim 0.01 E_{ex}$ that survives there. The former component is ascribed to the free $\mathbb{Z}_2$ vortex, while the latter one is ascribed to the $\mathbb{Z}_2$-vortex pairs. Our experimental data turn out to be consistent with the $\mathbb{Z}_2$-vortex theory.

The remainder of this paper is organized as follows. In Sec. II, we explain the material and the experimental method employed in the present paper. Our experimental results are presented in Sec. III. The experimental data are interpreted in Sec. IV, where their relation to the $\mathbb{Z}_2$-vortex theory and to earlier experimental measurements is discussed. Finally, Sec. V is devoted to a summary and concluding remarks. Some of the details of the experimental procedures are given in the Appendixes, i.e., the correction of the zero-energy position (Appendix A), the fitting in elastic-scattering scale (Appendix B), an examination of the dependence of the QENS signal on the integrated $|Q|$ range (Appendix C), and additional information about the fitting parameters (Appendix D).

## II. MATERIAL AND METHOD

$NaCrO_2$ is a promising candidate to realize the $\mathbb{Z}_2$-vortex phenomena, as described below. This material provides a quasi-2D Heisenberg-spin ($Cr^{3+}$: $S = 3/2$) system in a rhombohedrally stacked triangular lattice with predominant nearest-neighbor in-plane antiferromagnetic exchange coupling [23–25]. Neither magnetic long-range order nor a spin-glass transition is observed down to low temperatures. The specific heat exhibits a nonsingular peak around $T_{Cp} \simeq$ 41 K, with no other singular behavior [8]. The magnetic susceptibility also exhibits a broad maximum around 48 K. Neutron diffraction indicates that a spin arrangement is short range with its inplane correlation length less than 20 lattice spacings and is an approximately 120° structure [23]. Further, NMR and $\mu$SR experiments indicate an unconventional gradual freezing or slowing down of spin fluctuations below $T_{Cp}$, which has been ascribed to the possible $\mathbb{Z}_2$-vortex transition or crossover [8].

QENS experiments were performed on the time-of-flight near-backscattering spectrometer, DNA, located at beam port BL02, MLF, J-PARC spallation neutron source in Japan [26]. The high energy resolution of 0.004 meV and the energy range of $-0.03 < E < 0.10$ meV were obtained by using a Si 111 analyzer and pulse-shaping chopper rotating at 225 Hz with a 3 cm slit [high resolution (HR)], whereas the wide energy range of $-0.5 < E < 1.5$ meV with a moderate energy resolution of 0.015 meV was achieved without the pulse-shaping chopper [wide band (WB)].

A powder sample of $NaCrO_2$ was synthesized by a solid-state reaction method, in which a stoichiometric mixture of $Na_2CO_3$ and $Cr_2O_3$ was ground, followed by calcination at 900 °C for 12 h in a blend-gas flow of 99% Ar and 1% $H_2$ with intermediate grinding and pelletizing. Approximately 4.1 g of the sample were placed onto aluminum foil and shaped into a hollow cylinder with a thickness of 2 mm, a diameter of 12 mm, and a height of 50 mm in order to mitigate the neutron-absorption effects as much as possible. The cylinder was sealed in a thin aluminum container with He exchange gas that was placed under a cold head in a He closed-cycle refrigerator. The temperature $T$ was varied between 10 and 50 K. Slight deviations in the experimental zero-energy position caused by experimental conditions are corrected as explained in Appendix A.

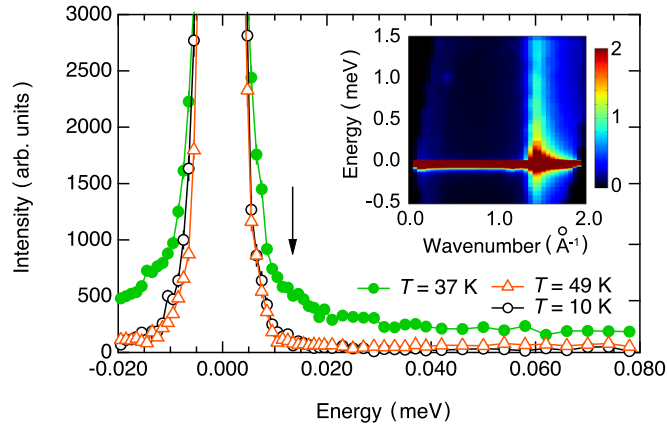


FIG. 1. Typical measured neutron-scattering spectra. The inset shows the overall distribution in the $Q$ and $E$ space, obtained at 37 K in the WB mode. The main panel shows the HR energy spectra measured at three temperatures. The arrow indicates the existence of QENS.

## III. EXPERIMENTAL RESULTS

In this section, we present the results of our QENS experiment. First, we check the overall picture of the intensity distribution in the wave number $Q$ and energy $E$ space in the WB mode, as shown in the inset in Fig. 1. The QENS signal is confirmed in $Q \approx 1.45$ Å$^{-1}$. Further, the main panel of Fig. 1 shows the representative QENS energy spectra in the HR mode measured at three representative temperatures, extracted by integrating the $Q$ range from 1.3 to 1.6 Å$^{-1}$. The QENS with the 0.01 meV order of quite narrow energy width almost disappears at low $T$ (10 K) and high $T$ (50 K) and grows at medium $T$ (37 K), as indicated by the arrow.

The fitting analysis of the QENS data is performed as follows. QENS intensity is generally described by

$$S(E) = \{C_{\rm el}\delta(E) + B(E)\chi''(E)\} \otimes R(E) + C_0, \qquad (1)$$

where $\delta(E)$ denotes the delta function for elastic incoherent scattering, $B(E)$ denotes the Bose population factor $[1 - \exp\{-E/(k_{\rm B}T)\}]^{-1}$, $\chi''(E)$ denotes the imaginary part of the generalized magnetic susceptibility, $R(E)$ denotes the resolution function, for which we use the data measured for the vanadium standard sample, $\otimes$ indicates the convolution integral by $R(E)$, and $C_0$ denotes the constant background.

For the HR data, we use the standard function

$$\chi''_{\rm HR}(E) = L_1(E) = C_1 \frac{E\Gamma_1}{E^2 + \Gamma_1^2}, \qquad (2)$$

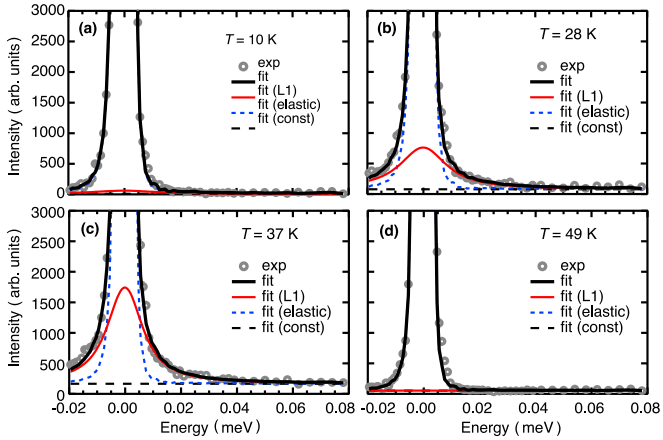


FIG. 2. Fitting results for HR QENS data measured at several temperatures. The symbols indicate the observed data, and the black solid curves indicate the calculated results. The red solid curves correspond to the QENS ($L_1$). The blue and black dashed lines correspond to the elastic incoherent scattering and the constant background, respectively. (a) $T = 10$ K, (b) $T = 28$ K, (c) $T = 37$ K, and (d) $T = 49$ K.

where $\Gamma_1$ denotes the energy width in the fluctuation function. The typical fitting results are shown in Fig. 2. Sufficiently good fitting is obtained for all the data. The fitting results for the HR data including the full elastic peak are also given in Fig. 5 in Appendix B, together with the residual errors. Sufficiently good fittings are also obtained in this scale, too.

For the WB data, in addition to the $L_1$ component with the 0.01 meV order width observed in the HR mode, another fluctuation component with 0.1 meV order width ($L_2$) is observed, as shown by gold lines in Fig. 3. Furthermore, the meV order component of spin-wave-like fluctuations was previously reported by higher-energy inelastic neutron scattering [25], and the present WB data widely cover the energy range with a maximum of $E = 1.5$ meV. Hence, the other meV order component ($L_3$) is also necessary. To be precise, the spin-wave-like component is not QENS, but the $Q$-integrated energy spectrum exhibits a profile similar to QENS [25]. Thus, it should be reasonable to use the following model consisting of three components:

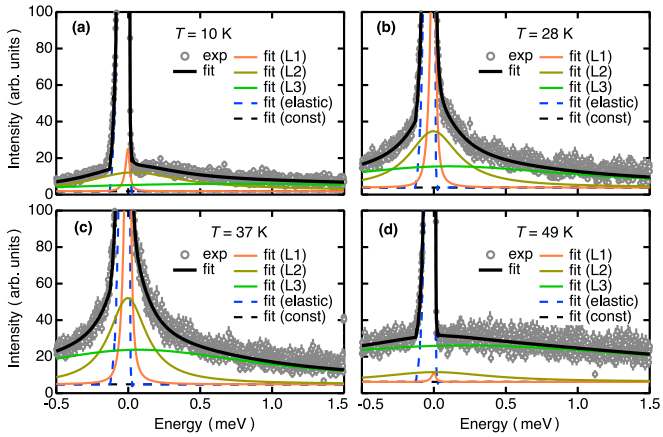


FIG. 3. Fitting results for WB QENS data measured at several temperatures. The orange, gold, and green solid curves correspond to QENS. The other symbols, solid curves, and dashed lines indicate the same as those defined in Fig. 2.

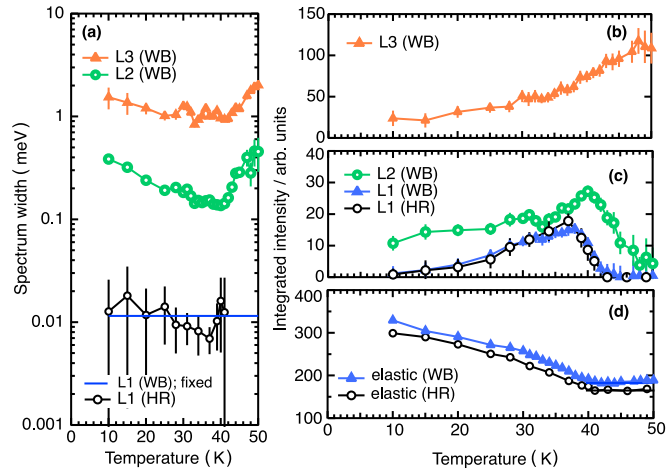


FIG. 4. Observed fitting parameters and their temperature dependences. (a) The spectrum widths $\Gamma_j$ ($j = 1$ to 3) are shown in logarithmic scale. Integrated intensities of (b) and (c) three fluctuation functions $L_j$ ($j = 1$ to 3) and (d) elastic components. The scales of arbitrary units are the same as those in Figs. 1 and 2 for HR and Fig. 3 for WB, while $L_1$ (HR) data in (c) and elastic (HR) data in (d) are multiplied by 0.54 and 0.44, respectively, for illustration.

$$\chi''_{\rm WB}(E) = \sum_{j=1}^{3} L_j(E) = \sum_{j=1}^{3} C_j \frac{E\Gamma_j}{E^2 + \Gamma_j^2}. \tag{3}$$

However, the 0.01 meV order $\Gamma_1$ is too small to redetermine by fitting the WB data. Therefore, it is better to use the values already obtained by fitting the HR data. Further, they exhibit no significant temperature dependence within the error bars, although they are somewhat rough, as shown in Fig. 4(a) below. Thus, we fix $\Gamma_1$ to the HR mean value, 0.012 meV. The typical fitting obtained is shown in Fig. 3. Sufficiently good fitting is obtained for all the data. The fitting results for the WB data including the full elastic peak are given in Fig. 6 in Appendix B, together with the residual errors. Sufficiently good fittings are also obtained.

In Figs. 1 and 2, we integrate the intensity of QENS for the relatively wide $Q$ region of $1.3 < |\boldsymbol{Q}| < 1.6$ Å$^{-1}$ to capture the whole magnetic signal at all temperatures even if the magnetic wave vector changes. To examine how the results depend on the integrated $|\boldsymbol{Q}|$ range, we also try a similar data analysis with a narrower $|\boldsymbol{Q}|$ range of $1.4 < |\boldsymbol{Q}| < 1.5$ Å$^{-1}$ for both the HR and WB data, and the results are given in Appendix C. As shown in Fig. 7, narrow QENS signals quite similar to the ones in Figs. 1 and 2 are obtained in the intermediate temperature range, demonstrating that our conclusion does not change with the $Q$ width of the integrated region.

We summarize the obtained spectrum widths and integrated intensities in Fig. 4. Figure 4(a) shows the three widths in a logarithmic scale, 0.01 meV order $\Gamma_1$, 0.1 meV order $\Gamma_2$, and 1 meV order $\Gamma_3$. The scale of the smallest $\Gamma_1$ corresponds to surprisingly slow spin fluctuations of $10^{-3}$ times the magnitude of exchange energy $E_{\rm ex} \approx 9$ meV and thermal

energy 40 K $\approx$ 4 meV, where $E_{ex}$ is estimated as $J_1 S(S+1)$, with nearest-neighbor antiferromagnetic exchange $J_1 = 2.4$ meV and spin $S = 3/2$; these values were reported by Curie-Weiss fitting in a magnetic susceptibility and inelastic neutron-scattering study of spin waves [24]. Further, $\Gamma_1$ exhibits no significant temperature dependence, as mentioned above. As the temperature decreases, $\Gamma_2$ decreases rapidly, bottoms around 40 K, and then increases slightly. The temperature dependence of $\Gamma_3$ is similar to that of $\Gamma_2$, but the degree of change is relatively small.

Figures 4(b)–4(d) show the temperature dependence of the integrated intensities of the fluctuation and elastic components. As the temperature decreases from 50 K, the $L_3$ fluctuation component with the largest integrated intensity in $L_1$, $L_2$, and $L_3$ monotonically decreases [Fig. 4(b)], and instead, the elastic component (nearly static and/or static) monotonically increases below 41 K [Fig. 4(d)], as normally expected for the critical slowing down of dynamics. In fact, the onset temperature, at which the nearly static component begins to rise, exhibits a systematic tendency with other experimental data in accordance with the energy resolution. Neutron diffraction (more than meV order of low resolution) exhibits an onset temperature of approximately 45 K, high-resolution elastic scattering (1 to 10 $\mu$eV order) of 41 K, and NMR and $\mu$SR ($\mu$eV to neV) of approximately 30 K [8]. That is, as the energy resolution becomes finer (timescale becomes slower), the onset temperature decreases.

In contrast, the behaviors of two $L_1$ and $L_2$ fluctuation components are nonmonotonic [Fig. 4(c)]. As the temperature decreases from 50 K, the $L_2$ intensity increases below 48 K, exhibits the maximum around 40 K, and then monotonically decreases but survives even at 10 K. The $L_1$ intensity increases below 43 K, exhibits the maximum around 37 K, then monotonically decreases, and almost disappears at 10 K. We also remark that the HR and WB temperature dependences of $L_1$ intensities are overlaid and are consistent with each other, supporting the validity of the fitting results. For completeness, we also show the temperature dependence of the constant background in Fig. 8 in Appendix D.

Thus, these QENS experiments succeed in capturing the characteristic spin fluctuations ($L_1$ and $L_2$ components), which are orders of magnitude slower than the energy scale of exchange coupling and thermal fluctuations and grow only in the critical temperature range between 20 and 50 K. In particular, the $L_1$ component is most enhanced around 37 K, which is clearly lower than specific-heat $T_{Cp} \simeq 41$ K. These features are different from normal ordering and critical scattering.

## IV. INTERPRETATION AND DISCUSSION

The most probable theory to describe the spin fluctuations in $NaCrO_2$ is the $\mathbb{Z}_2$-vortex model [2–5], as discussed, with circumstantial evidence, in Secs. I and II. Thus, we check the observed four components ($L_1$, $L_2$, $L_3$, and elastic) against this model.

First, this model also consists of mainly four components: (1) free $\mathbb{Z}_2$-vortex fluctuations, (2) $\mathbb{Z}_2$-vortex-pair fluctuations, (3) spin-wave-like fluctuations including paramagnons, and (4) a spin gel described by the essentially dynamic but nearly static short-range order with a 120°-based structure. The nearly static spin gel most likely corresponds to the elastic component. Spin-wave-like fluctuations also most likely correspond to the $L_3$ component, which was originally set with that in mind in Eq. (3). The overall temperature dependence, in which spin-wave-like fluctuations decrease [Fig. 4(b)] and the elastic spin gel instead grows on decreasing the temperature [Fig. 4(d)], is also natural both theoretically and experimentally.

The temperature dependence of the spectral width $\Gamma_3$ shown in Fig. 4(a), i.e., the spin-wave $L_3$ component including paramagnons, can be understood as follows. In general, as the temperature decreases towards the anomalous temperature in the high-temperature region, the spectral width of the paramagnons narrows due to the suppression of thermal fluctuations. In the low-temperature region below the anomalous temperature, where the well-defined spin-wave dispersion forms, the dispersion becomes a little steeper, and the pseudo density of states spectral distribution extends a little to the higher-energy side. Further, frustration causes the temperature range of these critical phenomena to expand. The spin-wave dispersion in $NaCrO_2$ becomes observable below around 40 K in inelastic neutron scattering [24]. Thus, all of these characteristics are consistent with the temperature dependence of $\Gamma_3$.

Next, we discuss whether components (1) and (2) of the $\mathbb{Z}_2$-vortex theory, i.e., the free $\mathbb{Z}_2$ vortex and the $\mathbb{Z}_2$-vortex pair, can be identified as the $L_1$ and $L_2$ components of the experiment. Theoretically, the $\mathbb{Z}_2$-vortex system is described by a topological number of $\mathbb{Z}_2$ vorticity, $z = 1$ and 0, where $z = 1$ denotes the free $\mathbb{Z}_2$ vortex and $z = 0$ denotes the $\mathbb{Z}_2$-vortex pair or no vortex. Ideally, only $z = 0$ is allowed below $T_V$, whereas both $z = 0$ and 1 are allowed above $T_V$. Interestingly, this kind of distinction is observed, as shown in Fig. 4(c). At the low temperature, $T = 10$ K, the $L_1$ component almost disappears, and the $L_2$ component finitely survives. At higher temperatures, both the components exist. Thus, the $L_1$ and $L_2$ components can be identified as the free $\mathbb{Z}_2$ vortex ($z = 1$) and the $\mathbb{Z}_2$-vortex pair ($z = 0$), respectively.

The earlier $\mu$SR study revealed that $T_1^{-1}$ exhibits a broad peak centered around 25–30 K, suggesting that low-energy spin fluctuations appear there, and survives at 10 K [8]. $T_1^{-1}$ is accompanied by the stretched exponent $\alpha = 0.5$, indicating a nontrivial distribution of $T_1^{-1}$ or of muon sites, which makes the interpretation of $T_1^{-1}$ difficult. The observation of the nonvanishing $T_1^{-1}$ even in the lower temperature range below around 10 K might come from the contribution of such a broad distribution of the relaxation time.

In the present QENS study, on the other hand, by using the DNA spectrometer with high energy resolution and with a wide energy range of three orders of magnitude from 0.003 to 1 meV [26], we have succeeded in directly observing the energy-resolved spin fluctuations over a wide energy range with the same spectrometer and under the same $Q$ range and experimental conditions, allowing us to capture an overall more resolved picture of spin fluctuations in comparison with the $\mathbb{Z}_2$-vortex theory. In this way, we have succeeded in decomposing low-energy spin fluctuations into two components, $L_1$, which vanishes at 10 K, and $L_2$, which survives there.

Of course, the type of expected anomalies might differ between the QENS and the $\mu$SR. Taking an example of simple

ferromagnets, an inflection point of the temperature vs magnetization (the order parameter of ferromagnets) curve can be employed as an experimental indicator of $T_c$, whereas the diverging point of the temperature vs the susceptibility curve can also be employed for that purpose. In our present case, the $L_1$-peak intensity of QENS represents the number of free $\mathbb{Z}_2$ vortices serving as the order parameter (or, rather, the disorder parameter) of the $\mathbb{Z}_2$-vortex ordering, while $T_1^{-1}$ of $\mu$SR corresponds to the dynamical susceptibility. Hence, one may expect the peak temperature of the $\mu$SR (or ESR) $T_1^{-1}$, which was reported to be $25 \pm 5$ K [8,14], to roughly correspond to the point at which the QENS $L_1$-peak intensity exhibits a sharp drop on decreasing $T$. Although it is difficult to identify a truly sharp anomaly in our data for the $L_1$ intensity, it appreciably decreases across 25 K on decreasing $T$, consistent with such an expectation. Of course, anomalous temperatures observed by different experimental probes with different energy scales do not necessarily agree, and such a correspondence should be regarded as a rough correspondence. For more precise estimation and deeper understanding of the vortex transition temperature, a future systematic QENS study for other $ACrO_2$ ($A$ = H, Li, Na) compounds might be helpful.

Thanks to the $\mathbb{Z}_2$ topological protection, an isolated free $\mathbb{Z}_2$ vortex is expected to be long-lived compared to the energy scale of the exchange coupling and thermal fluctuations, which is consistent with the observation of the narrow width of the $L_1$ component, $\Gamma_1 \sim \tau_1^{-1}$. However, the observed $\Gamma_1 \sim 0.001E_{\rm ex}$ is even narrower than the value expected from the previous spin-dynamics simulation of $\sim 0.01E_{\rm ex}$ [22]. In order to examine whether this amount of narrow width (long lifetime) is possible in the $\mathbb{Z}_2$-vortex scenario, we recently extended the earlier simulation of Ref. [22] to higher energy resolution (longer simulation time) and to larger lattices, finding that a width of $\sim 0.001E_{\rm ex}$ is indeed possible [27]. By contrast, a $\mathbb{Z}_2$-vortex pair consists of two nearby $\mathbb{Z}_2$ vortices that can destroy each other, which is consistent with the observation of a relatively large width (short lifetime) $\Gamma_2 \sim \tau_2^{-1}$ of the $L_2$ component, that is, a magnitude relationship of $\Gamma_1 < \Gamma_2$ ($\tau_1 > \tau_2$).

However, it may be only in the low-temperature range that the $L_1$ and $L_2$ components can be clearly decomposed as free and paired $\mathbb{Z}_2$ vortices, respectively. In simulations [2–4], at $T \gtrsim T_{Cp}$, the high-density free $\mathbb{Z}_2$ vortices spatially mingle with the $\mathbb{Z}_2$-vortex pairs with mutual collisions, and their lifetimes would be shorter and comparable to each other. Hence, around and above $T_{Cp} \sim 41$ K, the $L_2$ component is considered the mixture of $\mathbb{Z}_2$-vortex pairs and short-lived free $\mathbb{Z}_2$ vortices.

Further, in the higher-temperature range, as the $\mathbb{Z}_2$ vorticity itself becomes ill defined due to the loss of the minimum amount of short-range order, the $\mathbb{Z}_2$-vortex mixture would be indistinguishable from other high-energy excitations. This might be the reason behind our observation that the $L_2$ component goes away and only the $L_3$ component remains above around 50 K.

As argued above, although it is rather difficult to precisely estimate $T_V$ from the present QENS data, our data are consistent with the earlier $\mu$SR and ESR estimates of $25 \pm 5$ K [8,14]. We could also estimate $T_V$ from the $\mathbb{Z}_2$-vortex theory, giving the relation $T_V = 0.285E_{\rm ex} = 0.285J_1S(S+1)$ [2,4]. Using $J_1 = 2.4$ meV $= 28$ K, estimated by the meV order inelastic neutron scattering and spin-wave analysis [24], we obtain $T_V = 0.285 \times 28 \times (3/2)(3/2+1) = 30$ K. Using another value $J_1 = 20$ K [8], we obtain $T_V = 0.285 \times 20 \times (3/2)(3/2+1) = 21$ K. Thus, all the studies seem to suggest a $T_V$ value in the range of $25 \pm 5$ K.

Although the free $\mathbb{Z}_2$ vortices disappear below $T_V$ in theory, the corresponding $L_1$ intensity exhibits a low-$T$ tail below 25 K before vanishing around 10 K [Fig. 4(c)]. This rounding-off behavior might arise from either of the following two effects: (i) the nonideal effects in experiments (e.g., the impurities or defects might pin the free $\mathbb{Z}_2$ vortex at low $T$, the slow relaxation process in the spin-gel state below $T_V$ might hamper efficient pair annihilation of the far-apart free $\mathbb{Z}_2$ vortices) and (ii) the powder nature of the sample tending to make the $L_1$ peak of QENS "normalized," consisting of the contributions not only from the free $\mathbb{Z}_2$ vortex but also from the loosely bound $\mathbb{Z}_2$-vortex pair.

We wish to discuss point (ii) further in connection with a recent theoretical calculation [27]. Reference [27] suggested that the width and the intensity of the QENS peak vary with the wave vector $\boldsymbol{Q}$, becoming narrower as $\boldsymbol{Q}$ approaches the $K$ point, eventually being as narrow as $\sim 0.001J$, which is of the same order as the $L_1$-peak width. Such a narrow peak arising from $\boldsymbol{Q}$'s close to the $K$ point has been ascribed to the free $\mathbb{Z}_2$ vortex, while a bit wider peak arises from $\boldsymbol{Q}$'s slightly away from the $K$ point with the loosely bound $\mathbb{Z}_2$-vortex pair.

Since our sample is a powder, the $L_1$ peak of QENS might contain not only the contributions from $\boldsymbol{Q}$'s very close to the $K$ point but also those slightly away from the $K$ point. Yet theory has indicated that near $T_V$ the QENS intensity is dominated by the contributions from $\boldsymbol{Q}$'s very close to the $K$ point associated with the free $\mathbb{Z}_2$ vortex (see Fig. 1(c) of Ref. [27]), and consequently, a sharp QENS peak with a width of $0.001J$ would be visible even after the powder average, consistent with the present QENS observation.

In this way, the powder-averaged $L_1$-peak intensity might not be a contribution purely from the free $\mathbb{Z}_2$ vortex but rather might be a normalized one convoluted with the contribution from the loosely bound $\mathbb{Z}_2$-vortex pair. This raises an interesting possibility also for the temperature $T$ dependence of the experimental $L_1$-peak width. As $T$ is decreased toward $T_V$ from above, the number of both free $\mathbb{Z}_2$ vortices and $\mathbb{Z}_2$-vortex pairs would decrease, but at different rates, the former decreasing more strongly than the latter simply because only the former should vanish at $T_V$. While the peak width generally decreases with decreasing $T$ at a given fixed $\boldsymbol{Q}$, the aforementioned $T$ variation of the relative weights of different $\boldsymbol{Q}$'s would weaken the decrease of the peak width, which seems consistent with the experimental observation that the $T$ dependence of the $L_1$-peak width is rather weak.

From a theoretical perspective, the $\mathbb{Z}_2$-vortex physics is basically of a topological nature, rather insensitive to many details of the system. For example, the nature of the $\mathbb{Z}_2$-vortex order is expected to be insensitive to whether the underlying magnetic short-range order is either commensurate or incommensurate as long as it is noncollinear. Especially, since the spin-correlation length remains finite even below $T_V$, the $\mathbb{Z}_2$-vortex order is robust against weak perturbative interactions, e.g., the weak interplane coupling. In the case of our

target magnet $NaCrO_2$, neutron-scattering measurements by Hsieh *et al.* indicated that the in-plane translation vector became incommensurate below 30 K due to the effect of the weak interplane coupling [23]. The same measurements also indicated that three-dimensional magnetic order did not arise even below 30 K, with the interplane correlation length remaining only about four layers. This means that the system remains essentially 2D even below 30 K. Note that, concerning the ordering process or phase transition where the long-distance behavior is crucially important, four-layer system should still be regarded as a 2D system. Hence, it is theoretically expected that the same $\mathbb{Z}_2$-vortex physics applies to $NaCrO_2$, the only possible change being a deformation of the short-scale spin structure caused by the interplane interaction, which, however, maintains the $SO(3)$ topology, a crucial ingredient of the $\mathbb{Z}_2$-vortex physics.

## V. SUMMARY AND CONCLUDING REMARKS

In summary, by using a single spectrometer with a high energy resolution and wide energy band, we succeeded in clarifying the four components that construct the $\mathbb{Z}_2$-vortex theory prediction, i.e., a spin gel, free $\mathbb{Z}_2$ vortex, $\mathbb{Z}_2$-vortex pair, and spin wave. The $\mathbb{Z}_2$-vortex theory can naturally explain many experimentally observed characteristics, which verifies the $\mathbb{Z}_2$-vortex theory and its real materiality.

The $\mathbb{Z}_2$ vortex, although predicted a long time ago [2], has received relatively little attention until now. However, its new importance in terms of spintronics was also demonstrated by the recent theory in which this topologically protected spin texture can be a stable and efficient carrier of spin density [6]. Hopefully, the present results will promote further studies on the thermodynamic and transport properties of the $\mathbb{Z}_2$ vortex.

## ACKNOWLEDGMENTS

We thank Dr. Y. Kousaka for supporting the sample preparation. The neutron experiments were performed with the approval of J-PARC (Grant No. 2019A0295). This study was financially supported by MEXT and JSPS KAKENHI (Grants No. JP17H06137 and No. JP18K03503).

## APPENDIX A: FITTING OF ZERO ENERGY

In order to incorporate the slight deviations of the experimental zero-energy position $E_0$ caused by subtle differences in experimental conditions, for example, accelerator conditions, chopper speed fluctuations, and sample positions, we fit the $E_0$ value in each spectrum under the constraint that all the $E_0$'s of the $\delta$ function, $L_1$, $L_2$, and $L_3$, are identical. Precisely, QENS intensity is described by

$$S(E) = \{C_{\mathrm{el}}\delta(E') + B(E')\chi''(E')\} \otimes R(E') + C_0,$$
$$E' = E - E_0. \tag{A1}$$

In all the HR data, the obtained $E_0$ values are approximately only $4 \times 10^{-4}$ meV, and the difference among the spectra measured at different temperatures is only $3 \times 10^{-5}$ meV, which is negligible for both the typical $\Gamma_1$, $1 \times 10^{-2}$ meV, and the resolution, $4 \times 10^{-3}$ meV.

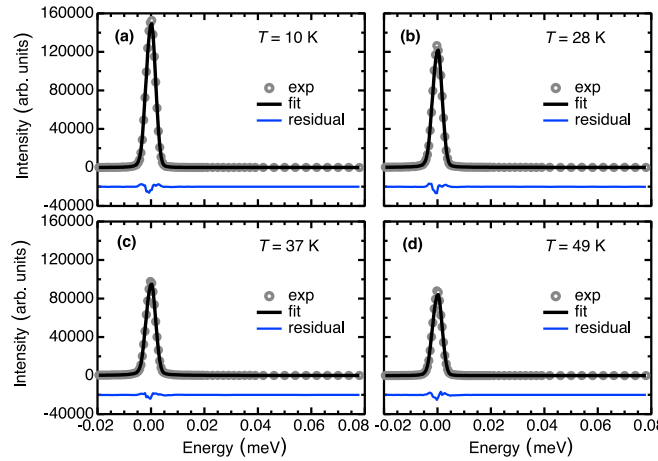


FIG. 5. HR data of the full elastic peak with residual errors. The symbols indicate the observed data. The black solid curves indicate the calculated results. The blue lines correspond to the residual errors. (a) $T = 10$ K, (b) $T = 28$ K, (c) $T = 37$ K, and (d) $T = 49$ K. The scales of arbitrary units are the same as those in Figs. 1 and 2 in the main text.

## APPENDIX B: FITTING IN ELASTIC-SCATTERING SCALE

Figures 5 and 6 show the HR and WB data for the full elastic peak with residual errors, respectively. Sufficiently good fittings are obtained in this scale, too.

The QENS signal is very weak compared to the elastic-scattering component, but the instrument used for the measurements (DNA) exhibits the world's highest signal-to-noise ratio (very low background) among similar instruments [26]. The signal-to-noise ratio of DNA reaches 100 000, which is nearly 100 times better than others, that is, the best in the world. This great performance allows for the fine fitting.

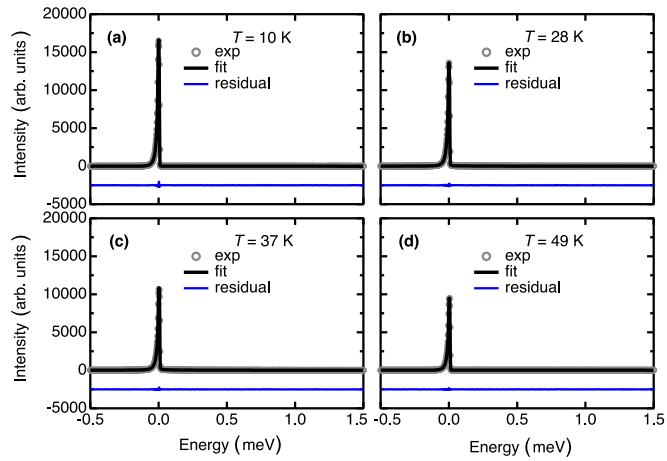


FIG. 6. WB data of the full elastic peak with residual errors. The symbols indicate the observed data. The black solid curves indicate the calculated results. The blue lines correspond to the residual errors. (a) $T = 10$ K, (b) $T = 28$ K, (c) $T = 37$ K, and (d) $T = 49$ K. The scales of arbitrary units are the same as those in Fig. 3 in the main text.

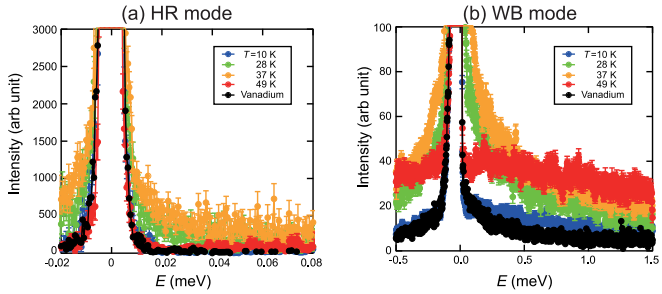


FIG. 7. Neutron-scattering spectra corresponding to the narrower $|\boldsymbol{Q}|$ range from 1.4 to 1.5 Å$^{-1}$ measured at four temperatures (a) in the HR mode and (b) in the WB mode.

The tail from the elastic peak on the negative-energy side in Fig. 6 is due to the tail of the neutron pulse for the wide-band mode, whereas the larger tail on the positive-energy side in Fig. 3 in the main text is due to QENS enhanced by the Bose factor.

## APPENDIX C: EXAMINATION OF THE DEPENDENCE OF THE QENS SIGNAL ON THE INTEGRATED $|Q|$ RANGE

In the main text, we integrate the intensity of QENS for the relatively wide $Q$ region of $1.3 < |\boldsymbol{Q}| < 1.6$ Å$^{-1}$ to capture the whole magnetic signal at all temperatures even if the magnetic wave vector changes. To examine how the results presented in the main text depend on the integrated $|\boldsymbol{Q}|$ range, we also try a similar data analysis with a narrower $|\boldsymbol{Q}|$ range of $1.4 < |\boldsymbol{Q}| < 1.5$ Å$^{-1}$, and the results corresponding to Fig. 1 in the main text are shown in Fig. 7. Intensities for vanadium data in these plots are normalized to the $T = 10$ K data at $E = 0$. In the high-resolution (HR) data, narrow QENS with 0.01 meV order ($L_1$) appears in the intermediate temperature range, which is consistent with Fig. 1. For the wide-band (WB) data, QENS with 0.1 meV order ($L_2$) also appears in the intermediate temperature range. Thus, our conclusion does not change with the $Q$ width of the integrated region.

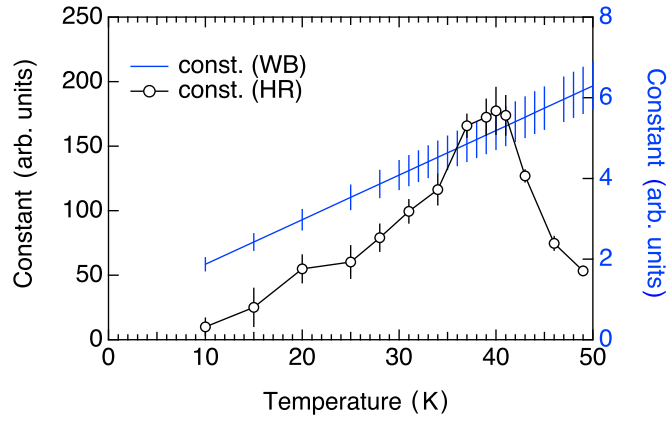


FIG. 8. The temperature dependence of the constant background parameters. The scales of arbitrary units are that same as those in Figs. 1 and 2 in the main text for the HR mode and in Fig. 3 in the main text for the WB mode.

## APPENDIX D: THE FITTING PARAMETERS

In Fig. 4 in the main text, we show the temperature dependence of the width of the $L_1$–$L_3$ peaks as well as the integrated intensity of the $L_1$–$L_3$ peaks and the elastic component. In this Appendix, we show for completeness the corresponding quantity for the constant background. Figure 8 shows the temperature dependence of the background parameters in the HR and WB modes. In the HR mode, the fitted background parameters exhibit a temperature dependence similar to that of the $L_2$ component. This is a quite natural result because the $L_2$ component identified in the WB mode is captured in the HR mode as a constant background due to the narrow energy range of the HR mode.

In the WB mode, a phononic background linearly proportional to the temperature should be considered in addition to the temperature-independent instrumental background. We obtained such a background, $a + b'T$, first at $Q = 0.8$ Å$^{-1}$, where no magnetic signal exists. Since the phononic background is proportional to $Q^2$, the background parameter $b$ at $Q_{\mathrm{mag}} = 1.45$ Å$^{-1}$ was estimated by multiplying $b'$ by the square of the ratio of $Q_{\mathrm{mag}} = 1.45$ to 0.8 Å$^{-1}$, and the results are shown in Fig. 8.


[1] J. M. Kosterliz and D. J. Thouless, J. Phys. C **6**, 1181 (1973).
[2] H. Kawamura and S. Miyashita, J. Phys. Soc. Jpn. **53**, 4138 (1984).
[3] H. Kawamura, J. Phys.: Conf. Ser. **320**, 012002 (2011).
[4] H. Kawamura, A. Yamamoto, and T. Okubo, J. Phys. Soc. Jpn. **79**, 023701 (2010).
[5] H. Kawamura and A. Yamamoto, J. Phys. Soc. Jpn. **76**, 073704 (2007).
[6] K. Aoyama and H. Kawamura, Phys. Rev. Lett. **124**, 047202 (2020).
[7] S. Nakatsuji, Y. Nambu, H. Tonomura, O. Sakai, S. Jonas, C. Broholm, H. Tsunetsugu, Y. Qiu, and Y. Maeno, Science **309**, 1697 (2005).
[8] A. Olariu, P. Mendels, F. Bert, B. G. Ueland, P. Schiffer, R. F. Berger, and R. J. Cava, Phys. Rev. Lett. **97**, 167203 (2006).
[9] S. Zhao, P. Dalmas de Réotier, A. Yaouanc, D. E. MacLaughlin, J. M. Mackie, O. O. Bernal, Y. Nambu, T. Higo, and S. Nakatsuji, Phys. Rev. B **86**, 064435 (2012).
[10] Y. Nambu, J. S. Gardner, D. E. MacLaughlin, C. Stock, H. Endo, S. Jonas, T. J. Sato, S. Nakatsuji, and C. Broholm, Phys. Rev. Lett. **115**, 127202 (2015).
[11] Y. Ajiro, H. Kikuchi, S. Sugiyama, T. Nakashima, S. Shamoto, N. Nakayama, M. Kiyama, N. Yamamoto, and Y. Oka, J. Phys. Soc. Jpn. **57**, 2268 (1988).
[12] H. Yamaguchi, S. Kimura, M. Hagiwara, Y. Nambu, S. Nakatsuji, Y. Maeno, and K. Kindo, Phys. Rev. B **78**, 180404(R) (2008).

[13] H. Yamaguchi, S. Kimura, M. Hagiwara, Y. Nambu, S. Nakatsuji, Y. Maeno, A. Matsuo, and K. Kindo, J. Phys. Soc. Jpn. **79**, 054710 (2010).
[14] M. Hemmida, H. A. Krug von Nidda, and A. Loidl, J. Phys. Soc. Jpn. **80**, 053707 (2011).
[15] W. Gao, L. Shi, Z. Ouyang, Z. Xia, Z. Wang, B. Liu, H. Li, Y. Zou, L. Yu, L. Zhang, L. Pi, Z. Qu, and Y. Zhang, J. Phys.: Condens. Matter **30**, 265802 (2018).
[16] H. Takeya, K. Ishida, K. Kitagawa, Y. Ihara, K. Onuma, Y. Maeno, Y. Nambu, S. Nakatsuji, D. E. MacLaughlin, A. Koda, and R. Kadono, Phys. Rev. B **77**, 054429 (2008).
[17] A. Yaouanc, P. Dalmas de Réotier, Y. Chapuis, C. Marin, G. Lapertot, A. Cervellino, and A. Amato, Phys. Rev. B **77**, 092403 (2008).
[18] D. E. MacLaughlin, Y. Nambu, S. Nakatsuji, R. H. Heffner, L. Shu, O. O. Bernal, and K. Ishida, Phys. Rev. B **78**, 220403(R) (2008).
[19] F. Xiao, T. Lancaster, P. J. Baker, F. L. Pratt, S. J. Blundell, J. S. Möller, N. Z. Ali, and M. Jansen, Phys. Rev. B **88**, 180401(R) (2013).
[20] H. Kadowaki, K. Ubukoshi, K. Hirakawa, and J. L. Martínez, and G. Shirane, J. Phys. Soc. Jpn. **56**, 4027 (1987).
[21] N. Kojima, K. Ito, I. Mogi, M. Takeda, G. Kido, Y. Nakagawa, M. Sakai, N. Kuroda, and Y. Nishina, J. Phys. Soc. Jpn. **62**, 4137 (1993).
[22] T. Okubo and H. Kawamura, J. Phys. Soc. Jpn. **79**, 084706 (2010).
[23] D. Hsieh, D. Qian, R. F. Berger, R. J. Cava, J. W. Lynn, Q. Huang, and M. Z. Hasan, Phys. B (Amsterdam, Neth.) **403**, 1341 (2008).
[24] D. Hsieh, D. Qian, R. F. Berger, R. J. Cava, J. W. Lynn, Q. Huang, and M. Z. Hasan, J. Phys. Chem. Solids **69**, 3174 (2008).
[25] D. Hsieh, D. Qian, R. F. Berger, C. Liu, B. Ueland, P. Schffer, Q. Huang, R. J. Cava, J. W. Lynn, and M. Z. Hasan, arXiv:1405.6184.
[26] K. Shibata, N. Takahashi, Y. Kawakita, M. Matsuura, T. Yamada, T. Tominaga, W. Kambara, M. Kobayashi, Y. Inamura, T. Nakatani, K. Nakajima, and M. Arai, JPS Conf. Proc. **8**, 036022 (2015).
[27] Y. P. Mizuta, K. Aoyama, K. Tomiyasu, M. Matsuura, and H. Kawamura, J. Phys. Soc. Jpn. **91**, 035001 (2022).